

Photovoltaic potential of tin perovskites revealed through layer-by-layer investigation of optoelectronic and charge transport properties

Mahmoud H. Aldamasy^{1†}, Artem Musiienko^{1*†}, Marin Rusu¹, Davide Regaldo², Shengnan Zho¹, Hannes Hampel¹, Chiara Frasca¹, Zafar Iqbal¹, Thomas W. Gries¹, Guixiang Li¹, Ece Aktas³, Giuseppe Nasti³, Meng Li⁵, Jorge Pascual⁶, Noor Titan Putri Hartono¹, Qiong Wang¹, Thomas Unold¹, Antonio Abate^{1,3*}.

1 Helmholtz-Zentrum Berlin für Materialien und Energie, 14109, Berlin, Germany.

2 Institut Photovoltaïque d'Ile de France, 30 Route Départementale 128, 91120, Palaiseau, France

3 Department of Chemical, Materials and Production Engineering. University of Naples Federico II. Naples, p.zz.le Vincenzo Tecchio 80, 80125, Naples Italy.

4 Egyptian Petroleum Research Institute, Nasr City, P.O. 11727, Cairo, Egypt.

5 Key Lab for Special Functional Materials of Ministry of Education, National and Local Joint Engineering Research Center for High-efficiency Display and Lighting Technology, School of Materials Science and Engineering, and Collaborative Innovation Center of Nano Functional Materials and Applications, Henan University, Kaifeng, 475004 China.

6 Polymat, University of the Basque Country UPV/EHU, 20018 Donostia-San Sebastian, Spain.

* corresponding author: artem.musiienko@helmholtz-berlin.de, antonio.abate@helmholtz-berlin.de

†These authors contributed equally to this work.

Abstract:

Tin perovskites are the most promising environmentally friendly alternative to lead perovskites. Among tin perovskites, FASnI₃ (CH₃NH₂SnI₃) shows optimum band gap, and easy processability. However, the performance of FASnI₃ based solar cells is incomparable to lead perovskites for several reasons, including energy band mismatch between the perovskite absorber film and the charge transporting layers (CTLs) for both types of carriers, i.e., for electrons (ETLs) and holes (HTLs). However, the band diagrams in the literature are inconsistent, and the charge extraction dynamics are poorly understood. In this paper, we study the energy band positions of FASnI₃ based perovskites using Kelvin probe (KP) and photoelectron yield spectroscopy (PYS) to provide a precise band diagram of the most used device stack. In addition, we analyze the defects within the current energetic landscape of tin perovskites. We uncover the role of bathocuproine (BCP) in enhancing the electron extraction at the fullerene C₆₀/BCP interface. Furthermore, we used transient surface photovoltage (tr-SPV) for the first time for tin perovskites to understand the charge extraction dynamics of the most reported HTLs such as NiOx and PEDOT, and ETLs such as C₆₀, ICBA, and PCBM. Finally, we used Hall effect, KP, and time-resolved photoluminescence (TRPL) to estimate an accurate value of the *p*-doping concentration in FASnI₃ and showed a consistent result of $1.5 \times 10^{17} \text{ cm}^{-3}$. Our findings prove that the energetic system of tin

halide perovskites is deformed and should be redesigned independently from lead perovskites to unlock the full potential of tin perovskites.

Introduction:

Perovskite materials demonstrated outstanding performance in various photovoltaic applications due to their optimum charge transport properties and tunable bandgap. With a record efficiency of 26%, perovskite solar cells (PSCs) have matured to the point where it stands on the threshold of commercialization^{1,2}. Nevertheless, these ambitions collide with several obstacles that may delay or, in the worst-case scenario, prohibit the commercialization of PSCs. Among those are lead toxicity and bioavailability^{3,4}, which would be considered an imminent danger in case of cells rupture or cleavage. In this context, tin is the most suitable lead substitute due to size and electronic similarity⁵. However, the best-performing tin halide perovskite solar cells (THPSCs) are 10% less efficient than their lead counterpart and even further behind regarding stability and reproducibility. One of the main causes of this regression is energy bands misalignment⁶.

Tin perovskites show a shallower valence band maximum (VBM) and conduction band minimum (CBM) than lead perovskites. As a result, the energy bands of the most widely used CTLs are misaligned with the VBM and CBM of tin-based absorber material^{7,8,9}. This energetic deformation produces high interfacial recombination rates and low charge extraction efficiency¹⁰. Consequently, tin perovskites show hampered photovoltaic performance compared to lead perovskites and their theoretical potential¹¹. Practically, the tin perovskites community first adopted the regular n-i-p architecture and relied on metal oxides such as TiO₂ and Nb₂O₅ as ETLs and Spiro-OMeTAD as HTL. However, it suffered from chemical and physical complexities due to the reactivity of metal oxides¹². With the emergence of fullerenes in PSCs¹³, tin perovskites converted into inverted p-i-n architecture depending on PEDOT as HTL due to its easy processability and good wettability, and C₆₀/BCP as ETL. The later structure was universally adopted and matured to the point that it delivered a PCE of over 14% regardless of the considerable energy mismatch at both interfaces^{14,15}. Therefore, it is crucial to manage the interfaces energetically to mitigate the interfacial losses to achieve efficiencies of over 20%.

Several approaches were adopted to achieve well-aligned CTLs with the absorber materials in tin perovskites, such as interface engineering using intermediate layers that form a cascading energy level to enhance energy alignment and improve extraction^{16,17}, for example, Wang et al., introduced an intermediate layer of ethylene ammonium bromide (EABr) and achieved a remarkable V_{oc} of 0.85 V. While Liyuan et al., implied a perovskite graded structure with a narrow bandgap perovskite in the bulk and a wide bandgap perovskite structure at the interface leading to enhanced charge extraction rates and a PCE of 11%¹⁸. Another similar strategy is to deposit a top thin film of molecules with a dual function of passivation and energy alignment regulation. The best-performing molecules so far were trifluoroacetamide (TFA) with a PCE of 11.7%¹⁹, 6-maleimido-hexanehydrazide trifluoroacetate with a PCE of 13.64%²⁰, and fullerene-n-butyl-pyridine (C₆₀-BPy)

with a PCE of 14.1%²¹, Furthermore, Hayase et al., deposited acetylacetone (AcAc) and Ethylenediamine (EDA) sequentially to enhance the band alignment and achieved a PCE of 13%²². Nevertheless, the ultimate solution to the interfacial energy losses in tin perovskites is finding new CTLs that align perfectly with the absorber material's CBM and VBM. Therefore, many theoretical studies tried to simulate the performance of different combinations of tin perovskites and different CTLs. The most promising simulation expected a potential PCE of 23% using FTO/ZnO/MASnI₃/CuSCN/CuI/Au as a device stack^{23,24,25,26,27,28}.

To transform such promising theoretical predictions into realistic devices, we must understand the effect of the energetic alignment between the absorber layer and selective layers on the charge extraction efficiency accurately. Such detailed studies are needed to fill the knowledge gap on the energy misalignment in tin perovskites. Despite the importance of such a topic, only few studies have been done to fill in this knowledge gap as far as we know. However, precisely measuring the energy levels and charge transfer rates at interfaces is challenging on thin film stacks. Moreover, the vacuum conditions and the energy beams could harm the sensitive tin perovskite films. Therefore, in this paper we utilized an ambient-pressure Kelvin probe (KP) and photoelectron yield spectroscopy (PYS) to construct a band diagram for the most prevalent tin perovskite device stack. Then, we measured the *p*-doping concentration in the prepared FASnI₃ films using the Hall effect, photoluminescence (PL), and KP to determine the *p*-doping concentration accurately. Furthermore, we use time-resolved surface photovoltage (tr-SPV) to study charge extraction in THPSCs^{29,30,31}. Using tr-SPV, we track the illumination-induced surface potential and the direction of the photo-excited charges, which enables to investigate the charge carrier extraction rates at interfaces using different charge transporting layers (CTLs), including surface self-assembled monolayers (SAMs)³². Furthermore, we provide a quantitative analysis of charge extraction efficiency and the mechanisms responsible for charge loss by conducting charge extraction and recombination simulations. Then we quantify the loss mechanisms in FASnI₃ and compare it to similar lead perovskite structure. Finally, we simulate the effect of doping concentration on the device parameters and conclude the optimum parameters to enhance the efficiency of tin perovskites.

Results and Discussion:

Doping concentration of FASnI₃:

The accurate estimation of the *p*-doping level is vital for understanding the energetic landscape and charge carrier dynamics in tin perovskites. However, the degree of *p*-doping in FASnI₃ is not accurately measured, and the values reported in the literature range from 10¹⁵-10¹⁸ cm⁻³ using 10% SnF₂^{33,34}. As a result, we decided to measure the *p*-doping (hole concentration) in neat FASnI₃ using three different techniques: Hall effect, PL, and KP-PYS. **Figure 1a and b** show the hole concentration of prepared FASnI₃ with 10% SnF₂. The Hall effect and PL techniques show the same concentration (1.5 * 10¹⁷ cm⁻³). In strong agreement with these values, on freshly prepared FASnI₃ thin films on

quartz glass and ITO substrates, the KP-PYS measurements reveal hole concentrations of $1.9 \times 10^{17} \text{ cm}^{-3}$ and $1.3 \times 10^{17} \text{ cm}^{-3}$, respectively. Those values are calculated with the determined E_F - E_{VBM} energies of 0.01 eV and 0.08 eV from KP-PYS measurements (see next chapter) and hole effective mass in FASnI_3 of $0.05 m_0$ as reported in this reference³⁵. The consistency of the measured hole concentration from Hall effect, PL, and KP-PYS demonstrates that the $0.05 m_0$ hole effective mass published by Xie et al., is the most accurate value compared to the other calculated or measured values³⁵.

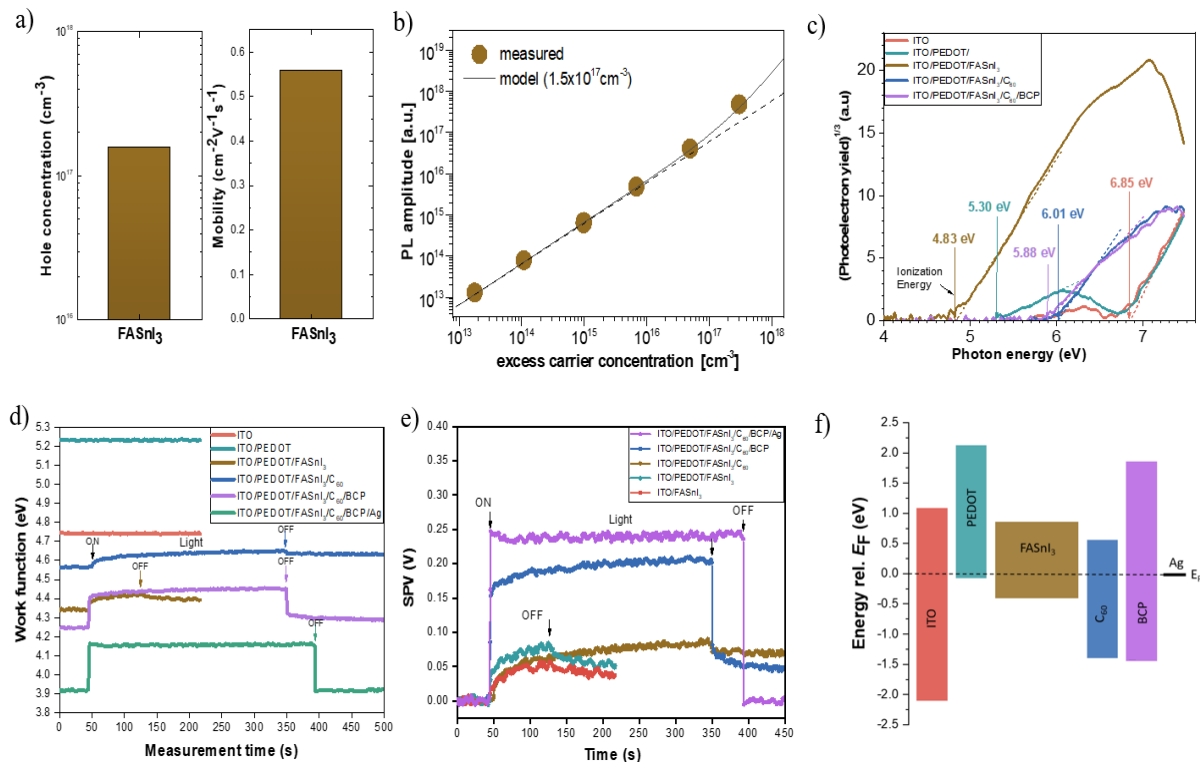


Figure 1: The electronic and energetic landscape of the ITO/PEDOT/FASnI₃/C₆₀/BCP/Ag solar cell. (a) Charge carrier concentration and mobility of FASnI₃ thin films. (b) Doping concentration determined by fitting the PL amplitude as function of excess carrier concentration from TRPL measurements. (c) Photoelectron yield spectra of each layer of the ITO/PEDOT/FASnI₃/C₆₀/BCP/Ag device stack with the revealed ionization energies from layer-by-layer studies. (d) Time-dependent work function measurements in the dark and under illumination as measured layer-by-layer from ITO to the complete solar cell stack using KP (On and Off refers to the start and the end of illumination). (e) Surface photovoltage (SPV) development from the ITO film to the complete device stack ITO/PEDOT/FASnI₃/C₆₀/BCP/Ag revealed by KP layer-by-layer measurements. (f) The energy band diagram of the ITO/PEDOT/FASnI₃/C₆₀/BCP/Ag structure with respect to Fermi level (E_F) plotted based on the data determined from KP and PYS measurements.

Energy band diagram of the ITO/PEDOT/FASnI₃/C₆₀/BCP/Ag solar cell:

To understand the efficiency losses related to CTLs in THPSCs, we analyze the interfacial energy bands alignment between the absorber layer and different CTLs in addition to the charge carrier extraction dynamics. The determined positions of the conduction and valence bands of different tin perovskite compositions and CTLs scatter significantly in the literature. This is partly explained by the difficulty of getting consistent measurements due to challenges like Sn²⁺ sensitivity to oxygen, beam damage during high-energy photoelectron analysis, and composition changes under high vacuum conditions. We have therefore performed the KP-PYS measurements under an inert N₂ atmosphere under normal conditions and using low energy photons between 3.4 – 7.5 eV. Based on these measurements, we build the band diagram for the studied ITO/PEDOT/FASnI₃/C₆₀/BCP/Ag solar cell device. The Fermi level position is found from work function measurements by KP (**Figure 1d**), and the band bending and the contribution of each layer to the solar cell V_{oc} are found from the magnitude of the SPV signal derived from KP data in the dark and under illumination (**Figure 1e**). The VBM position is determined as the ionization energy found from PYS spectra which were found by linear regression and extrapolation of the Y^{1/3}(hν) curves in **Figure 1c**, except that of Ag which was determined separately from Y^{1/2}(hν) plots valid for measurements on metals as shown in **Figures SI 1-4**. Knowing the VBM position, the CBM position is found by adding the band gaps of the respective thin films to the E_{VBM}. Assuming flat band conditions under the used 100 mW/cm² illumination, the doping concentration of the films is calculated. It is worth mentioning that the PYS measurements for the determination of the ionization energy (E_i) and the KP measurements for the determination of the work function (WF), which determines the Fermi level (E_F) position with respect to the vacuum level, were performed with the same Kelvin tip on the same sample position. Note that the work function of the KP tip was checked each time before starting a new measurement. It is worth mentioning that repeatedly performed PYS measurements have delivered the same ionization energy values denoting the chemical stability of the investigated thin film surface^{36,7,37,38,39}.

Figure 1d shows the layer-by-layer work function measurements in the dark and under illumination of the THPSC device. The measurements were stable and reproducible over the time, proving the prepared films' surface chemical and electrical stability. The light-induced work function variations in **Figure 1d** and the corresponding surface photovoltage (SPV) development in **Figure 1e** were first observed after the deposition of the FASnI₃ film. Since no SPV was recorded from ITO and PEDOT films, the observed SPV amplitude of about 70 mV is attributed to the potential barrier at the FASnI₃ film surface due to band bending. The C₆₀ layer, although deposited as an ETL on top of the FASnI₃ absorber film, did not enhance the SPV amplitude. Note that the SPV measured from a single film shall be attributed to the surface band bending, while an SPV measured from a *p-n* junction shall coincide with the open-circuit voltage (V_{oc}) of the solar cell device. With well passivated interfaces and appropriate contacts, the V_{oc} of a photovoltaic device shall approach the internal voltage (related to quasi-Fermi-level separation) within the absorber^{40,41}. It can be therefore concluded that the C₆₀ layer has no contribution to the built-in voltage within the FASnI₃ absorber. The SPV of the device stack increases significantly only after the deposition of the next BCP film. A further increase of SPV is observed after the deposition of a semitransparent 7-nm-thick Ag layer. Note that since the sample is illuminated through

the Ag film, the intensity of the incident light is significantly decreased and thus the recorded SPV deviates essentially from the potentially maximum achievable SPV signal. Nevertheless, these results show that the internal voltage within the FASnI₃ absorber increases essentially after the BCP deposition while reaching its maximum after the completion of the device structure by the back Ag film. It can be observed in addition from **Figure 1e** that a sharp increase of the SPV to its maximum value by switching on the light and a sharp decrease of the SPV after switching off the illumination occurs only after completing the solar cell stack by the Ag film. This shows that an optimum charge separation occurs at the back contact after the Ag film deposition. Although the SPV curve for the BCP completed device demonstrates an improved transfer of electrons from the absorber film to the BCP surface, long SPV relaxation time after the illumination is switched-off denote the presence of surface trap states.

With the data obtained from KP and PYS measurements, we plot the complete band diagram of the ITO/PEDOT/FASnI₃/C₆₀/BCP/Ag device stack under study aligned to the Fermi level in **Figure 1f** for discussion of the current transport, and aligned to the vacuum level in **Figure S15** for collecting the data on electron affinity (EA), Fermi level position and ionization energy of all the films in the device stack. The Fermi level aligned band diagram reveals the offsets of the energy levels at the perovskite CBM /HTL and at the perovskite VBM/ETL interfaces. Those band offsets influence both the charge carrier extraction and recombination. For the FASnI₃/PEDOT interface we calculate a positive band offset $\Delta E_v = 0.42$ eV by using $\Delta E_v = (E_F^{\text{pero}} - E_i^{\text{pero}}) - (E_F^{\text{HTL}} - E_i^{\text{HTL}})$. Thus, under assumption of a low density of recombination states at this interface, an effective extraction of holes from the FASnI₃ absorber would be expected. However, the extraction of holes into the degenerated ITO film bulk will be hindered by its superficial layer which looks intrinsic, as depicted in **Figure 1f**. At the FASnI₃/C₆₀ interface we calculate a negative band offset $\Delta E_c = -0.30$ eV by using $\Delta E_c = (EA^{\text{ETL}} - E_F^{\text{ETL}}) - (EA^{\text{pero}} - E_F^{\text{pero}})$. Consequently, there are no barriers present for an effective extraction of electrons at this interface. However, since the SPV signal differed only slightly compared to that of the FASnI₃ film and increased slowly under illumination while showing a long decay tail after the light switch-off, we assume a high density of trap states at this interface. The band structure of the BCP, as aligned to the C₆₀ energy levels, suggests a large barrier for extraction of electrons. Considering the essential increase of the SPV signal with the addition of the BCP layer, one can assume the electronic transport through the BCP film as assisted by gap states. Our KP-PYS studies show however that the chemistry and electronics of the BCP film is strongly influenced by the deposition on its top of the Ag layer, as we demonstrate in the next chapter.

The electronic structure of the BCP/Ag interface:

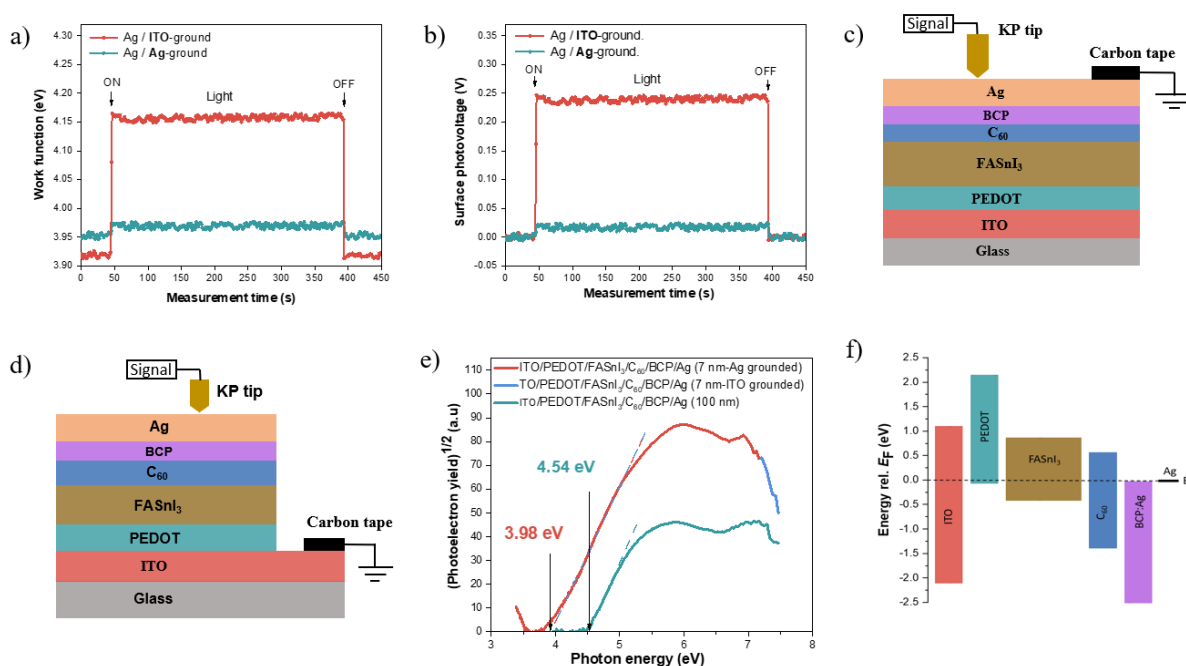


Figure 2: Electronics of the Ag/BCP interface. (a) Work function and (b) surface photovoltage of the ITO/PEDOT/FASnI₃/C₆₀/BCP/Ag device from KP measurements by selectively grounding either the ITO or Ag films. (c) Schematic diagram of the KP-PYS Ag-grounded sample. (d) Schematic diagram of the KP-PYS ITO-grounded sample. (e) Photoelectron yield spectra of a 7-nm-thick Ag film on top of the BCP layer measured by grounding the device stack either on the ITO or Ag films. (f) Proposed energy band diagram with a BCP:Ag blend layer with a LUMO level of 4.0 eV.

The BCP layer was inserted as a buffer layer between the ETL and the cathode to give rise to a cascade of energy levels for improved extraction of electrons and to create simultaneously a wide hole injection barrier that reflects holes and thus preventing the interface recombination⁴². However, the remarkable enhancement of the device SPV caused by the BCP/Ag stack motivated us to investigate the BCP/Ag interface to understand the origin of such an enhancement from the electronic point of view. Therefore, we prepared an entire device stack with a top Ag film of only 7 nm thickness. We carried out the KP measurements in the dark and under

illumination by grounding the ITO film in the first measurement, while in the second measurement, we grounded the Ag film as shown in **Figures 2a-d**. In both cases, the KP-PYS measurements were performed on the same sample position. Note that in the case of grounded ITO, the signals were recorded relative to the E_F of the ITO thin film, while in the case of grounded Ag, the signals were recorded with respect to the E_F of the Ag layer.

From the dark KP measurements (**Figure 2a**), we observe almost similar W_F values between 3.92 eV and 3.95 eV for both types of sample grounding. At the same time, from the PYS measurement (**Figure 2e**), we identify E_i value of 3.98 eV in both cases. These results show that the W_F of an investigated thin film on a solar cell stack is properly determined by KP measurements, independently of whether the measurement is conducted by grounding the solar cell's ITO (bottom) contact or directly on the measured top layer. The SPV of the Ag-grounded measurement (**Figure 2b**) is attributed to the (minor) surface band bending of the top layer, while the SPV of the ITO-grounded plot is attributed to the V_{oc} of the stack, related to the Fermi level splitting due to generation of charge carriers under illumination in the $FASnI_3$ absorber thin film. Thus, both KP (dark) and PYS measurements reveal similar W_F and E_i values, respectively, as would have been expected for a measurement on a metal or a degenerated semiconductor. However, the measured value of about 4.0 eV is (i) by 0.56 eV lower than that of the 100 nm thick Ag reference film (**Figure 2e**), (ii) by 0.25 eV lower than the E_F of BCP and (iii) by 1.88 eV lower than the E_{i-BCP} ^{43,44,45}. We suggest therefore that the early deposited Ag diffuses into BCP layer, forming a BCP:Ag blend with a W_F of around 4 eV, which is in an optimum position for effective electron extraction from C_{60} .

Lately, the concept of Ag:BCP blend layer was introduced by Ying et al. in tandem⁴⁶ and single junction⁴⁷ devices as a mediator between C_{60} and indium-zinc oxide (IZO) as a transparent electrode. The target was to protect the C_{60} layer from the sputtering damage during the deposition of the top conductive electrode. They proved the formation of a charge transfer Ag:BCP complex through coordinate covalent bonds between Ag and N atoms of BCP during the evaporation process. Similar interactions between BCP and electrodes with a different metal such as Mg were also reported⁴⁸. Ying et al. suggested that Ag:BCP complex forms gap states which work as channels to facilitate electrons transportation to the electrode. However, our investigation on the BCP/Ag interface reveal similar energies of about 4.0 eV for the work function and ionization energy. Such findings indicate the formation of a degenerated BCP:Ag surface layer. Therefore, we propose that the BCP:Ag is a complex with a Fermi level coinciding with its CBM position at 4.0 eV. This low work function contact layer to C_{60} provides a downward bending of the C_{60} bands, thus enabling a smooth transfer of electrons from C_{60} to the back Ag electrode, as shown in **Figure SI 6**. Conclusively, we suggest a modified energy band diagram as indicated in **Figure 2f**, in which BCP:Ag blend with a $W_F \approx 4$ eV replaces the traditional BCP layer.

Charge extraction dynamics at charge selective contacts:

Charges dynamics at the HTM buried interfaces:

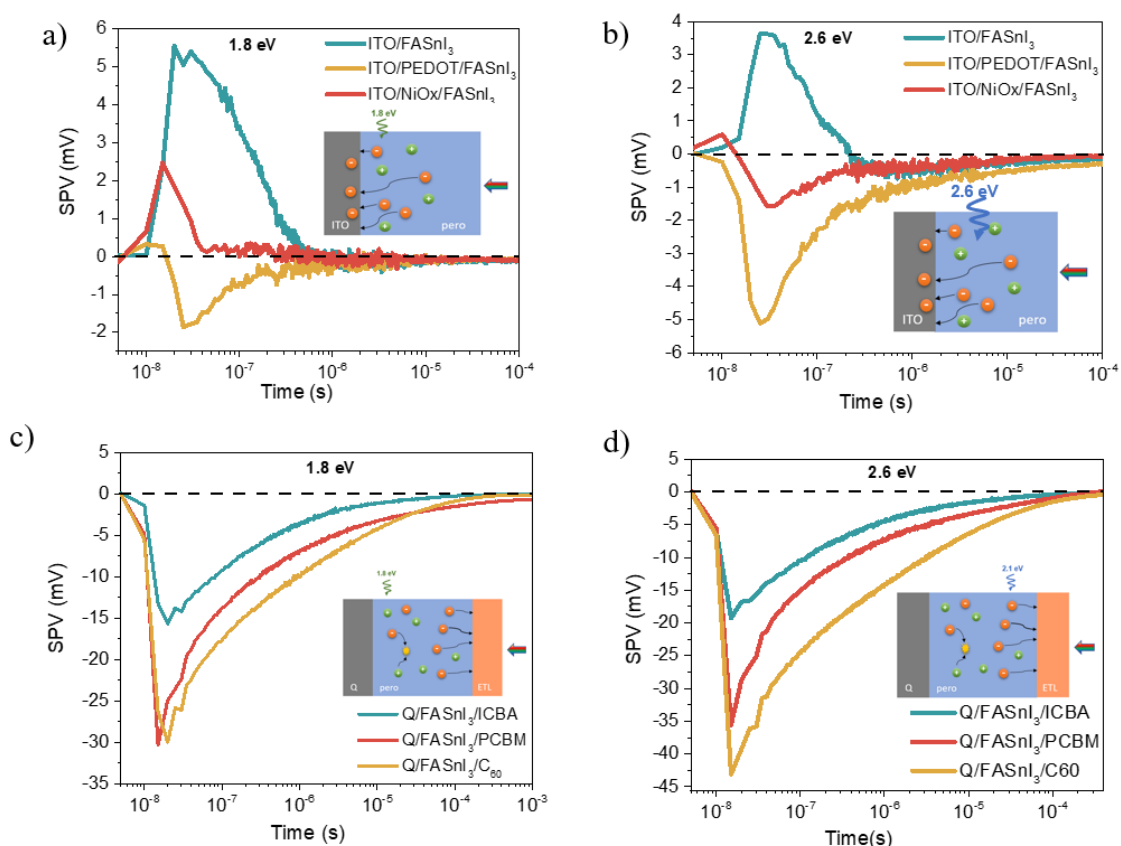


Figure 3: Free electron and hole extraction dynamics in different ETL and HTL interfaces of THPSCs a & c) excitation using 688 nm laser pulse (1.8 eV), which penetrates around 210 nm in a 250 nm thick film and excites electrons near the buried interface. b & d) Excitation using a 486 nm laser pulse (2.6 eV) penetrating up to 90 nm and excites electrons in the bulk of the perovskite film.

After illustrating the energetic landscape in the most common THPSC stack, we investigate different CTLs' ability to extract charges from the absorber layer by measuring tr-SPV. We illuminated the interfaces under

study from the top side, as shown in **Figure 3** insets with above-bandgap photon energy, and recorded charge dynamics from 5 ns to 1 ms. **Figures 3a & b** insets show the tr-SPV diagram of neat FASnI₃ at two different excitation energies, 1.8 eV and 2.6 eV, corresponding to penetration depths 210 and 90 nm, respectively, as indicated in **Figure SI 7**. The sign of the SPV signal reflects the electron or hole separation in space. A positive (negative) sign of transient reflects the electron (holes) separation for the bulk of the thin film to its surface or interface, leaving the perovskite film positively (negatively) charged³². The amplitude and rise rate of the signal indicate the amount of the separated charges and thus express the quality of charge extraction. The subsequent signal decrease indicates the recombination losses of the separated charge carriers. More experimental details can be found on **SI page 3 and Figure SI 8**.

We start by measuring the ability of ITO to extract charges directly from the FASnI₃ layer without any CTL in between. We found that ITO/FASnI₃ interface shows a positive tr-SPV signal, which indicates an electron accumulation near/in ITO, as shown in **Figures 3a & b**. The peak signal decreased when we generated carriers further away from the interface with 2.6 eV photons (**Figure 3b**). This electron accumulation can be attributed to the electron trapping or transfer in ITO, as similar effects were observed in ITO/lead perovskite interface previously³². Further, we explore hole extraction dynamics in FASnI₃/HTLs interfaces. In contrast to ITO/FASnI₃, PEDOT/FASnI₃ interface shows negative signals across the perovskite film, revealing holes extraction in PEDOT. However, the signal is stronger when we generate carriers deeper in the bulk of the perovskite film (**Figure 3b**) than closer to the interface (**Figure 3a**). This change in amplitude demonstrates a high interfacial recombination rate or barrier at the PEDOT/FASnI₃ interface. This draws our attention to the significance of the interfacial passivation and alignment of the buried interface in THPSCs^{49,50}. Notably, PEDOT shows a small positive signal at the beginning, an early electron trapping across the interface before 10 ns, which is shortly overflowed by hole extraction (**Figure 3a**). This indicates that the process of charge extraction at the PEDOT/FASnI₃ interface is derived by a competition between two processes, hole extraction, and electron trapping, which could be attributed to energy bands misalignment and low charge selectivity of PEDOT. Nevertheless, The hypothesis on electron trapping is in perfect agreement with data measured at 2.6 eV for the PEDOT interface (**Figure 3b**), where we did not observe any positive signal as a result of electron-hole generation and recombination far from the PEDOT interface and prevailed majority free hole drift in the bulk of the p-type material⁵¹.

Next, we study the hole extraction capabilities of NiOx and two carbazole-based self-assembled monolayers (2PACz and MeO-2PACz), which previously showed³² advanced hole extraction capabilities in lead-based perovskite cells and were also tried for tin perovskites⁵². The tr-SPV transient of NiOx shows a much less intense negative signal and much worse hole extraction capabilities than PEDOT. When free carriers are generated closer to the interface (with 1.8 eV photon), electron accumulation at the NiOx/FASnI₃ interface dominates, giving rise to a positive tr-SPV signal, as indicated in **Figure 3a**. At the same time, hole extraction becomes apparent only at 2.6 eV illumination, which is still affected significantly by the positive signal for electron accumulation. The detailed qualitative interpretation of charge transport for the NiOx interface is given in

Figure SI9. On the other side, only 2PACz showed signs of hole extraction at 2.6 eV illumination among SAMs, as shown in **Figures SI10a & b**. Similar to NiO_x, SAMs showed electron accumulation and low extraction capabilities compared to PEDOT. To validate the alignment effect on the hole extraction by SAMs, we added 20% SnBr₂ to deepen the valence band of tin perovskite⁷. Interestingly, we observe the improvement of hole extraction by NiO_x, 2PACz, and MeO-2PACz, which proves such HTLs could work with tin perovskites if the energy bands are appropriately aligned. In conclusion, these HTLs can be optimized for tin-perovskites with a broader bandgap for lead-free tandem applications.

Electron extraction dynamics at THPSCs:

To explore electron extraction dynamics at perovskite/ETLs interfaces, we measured the tr-SPV of ICBA, PCBM, and C₆₀ deposited on top of FASnI₃ as depicted in **Figures 3c-d**. In this structure, we illuminate from the top side. Hence, the higher excitation energy (2.6 eV) generates charge carriers close to the interface, while the lower energy laser (1.8 eV) excites near the bulk of the film, as shown in the inset of **Figure 3c-d**. We observe negative signals for all ETLs, which indicate an active electron extraction at the interface. The rapid increase in the signal amplitude suggests fast separation dynamics of electrons towards the ETL. Generally, C₆₀ shows a better extraction especially when we excite near from the interface. Interestingly, the charges extraction rate of the three ETLs follows the same order of charges mobility, which is 1.6 cm² V s⁻¹, 6.1 × 10⁻² cm² V s⁻¹, and 16.9 × 10⁻³ cm² V s⁻¹ for C₆₀, PCBM, and ICBA respectively not the order of the CBO values. This correlation can explain the superior performance of the C₆₀-based devices regardless of the unmatched energy bands compared to ICBA and PCBM keeping in mind also the vital role of BCP when coupled with C₆₀ to form one ETL as explained in a previous section⁵³. In addition, the C₆₀ interface (as well as other ETLs) shows a much larger peak amplitude of the signal (-47 mV) than the PEDOT interface (-5 mV), which reveals much better electron extraction capabilities compared to holes. This finding is surprising because electrons, which are minor carriers, are heavily influenced by empty traps in p-type doped FASnI₃. Therefore, one would expect a lower amplitude of tr-SPV signals for ETLs interfaces than HTLs interfaces. This observation directly highlights one of the bottlenecks in the state-of-the-art THPSC-HTL interface.

To simultaneously investigate electron and hole extraction, we conducted a comparison of time-resolved surface photovoltage (tr-SPV) for the sample with both the electron transport layer (ETL) and hole transport layer (HTL), as depicted in **Figure SI10**. The results demonstrate a significant enhancement in the extracted charges, with the tr-SPV signal's amplitude (-80 mV) several times larger than the combined signals of the pure ETL and HTL. This notable increase in the tr-SPV peak amplitude signifies the strong correlation between electron and hole extraction and highlights the substantial recombination losses caused by unextracted carriers. As carrier recombination occurs through various channels, including nonradiative, surface, and radiative pathways, a more in-depth discussion is provided in **supplementary note 1** and **Figure SI11**.

Simulation of charge extraction and recombination in tin perovskite interfaces

Previously in this manuscript, we qualitatively demonstrated charge transport dynamics in tin perovskite interfaces using various ETLs and HTLs. In this section, we provide a quantitative analysis of charge extraction efficiency and the mechanisms responsible for charge loss by conducting charge extraction and recombination simulations. We simulate charge transport in the interfaces that exhibit the highest charge extraction efficiency in tin perovskites and compare the quality of charge extraction with similar interfaces of lead perovskites, $(\text{CS}_{0.05}\text{FA}_{0.855}\text{MA}_{0.095})\text{Pb}(\text{I}_{0.9}\text{Br}_{0.1})_3$ with a power conversion efficiency of 22%. This comparison gives insights into the primary mechanisms causing charge losses and provide valuable information for developing future strategies to enhance THSPCs and other optoelectronic devices.

There are two channels for charge loss: radiative and non-radiative recombination. Radiative recombination rate ($C_b \cdot \Delta n(t) \cdot (\Delta p(t) + p_0)$) is influenced by the background hole concentration p_0 . The total Non-radiative recombination ($\frac{\Delta n}{\tau_{non-rad,e}}$ and $\frac{\Delta p}{\tau_{non-rad,h}}$) consists of bulk ($\frac{\Delta n}{\tau_{bulk,e}}$), surface ($s_e \cdot \Delta n$ and $s_h \cdot \Delta p$), and interface contributions ($s_{ie} \cdot \Delta n$ and $s_{ih} \cdot \Delta p$), as demonstrated in Eq. S1-2. $\Delta n(t)$ and $\Delta p(t)$ represent photogenerated electrons and holes, respectively. s_e and s_h are non-radiative surface recombination rate at the perovskite surface and s_{ie} and s_{ih} at the HTL and ETL interface. We consider these recombination channels as key factors governing charge dynamics in perovskite interfaces, along with electron and hole extraction rates $K_e \cdot n(t)$ and $K_h \cdot p(t)$, where K_e and K_h denote the coefficients for electron and hole extraction rates, respectively, as shown in Equations 1&2 and Figure 4a. Further details regarding the model can be found in SI equations S1-S4.

$$\frac{d\Delta p}{dt} = -K_h \Delta p + K_{hb} \Delta p_{HTM} - C_b ((\Delta p + p_0) \Delta n) - \frac{\Delta p}{\tau_{non-rad,h}} \quad (1)$$

$$\frac{d\Delta n}{dt} = -K_e \Delta n + K_{eb} \Delta n_{HTM} - C_b ((\Delta p + p_0) \Delta n) - \frac{\Delta n}{\tau_{non-rad,e}} \quad (2)$$

We initially employed the Levenberg-Marquardt method^{32,54} to fit the experimental data of $\text{FASnI}_3/\text{C}_{60}$ and $\text{FASnI}_3/\text{PEDOT}$, aiming to determine the rate constants that best align with the experimental tr-SPV results. The fit results are presented in **Figure 4b** and **Table S1**, while the time evolution of electrons, holes, and extracted electrons is depicted in **Figure 4e**. Subsequently, we performed a similar fitting process for the electron and hole extraction dynamics in lead perovskites. We utilized tr-SPV measurements conducted under identical conditions, as shown in **Figures 4c, f**, and **Table S1**. Careful examination of the charge extraction dynamics reveals a direct correlation between the rise of the tr-SPV signal in time (**Figures 4b and c**) and a reduction in carrier concentration (**Figures 4e and f**) within the perovskite film. This reduction is a consequence of the charge extraction process, leading to an increase in the extracted electron concentration in ETL and HTL. The further decay of tr-SPV and the maximum amplitude of the tr-SPV signal is significantly influenced by radiative and nonradiative recombination processes that tend to diminish the overall carrier density.

According to the simulation results, we observe significant differences in both charge extraction and recombination between lead and tin perovskites. The lead perovskite system exhibits lower recombination losses, resulting in a longer carrier lifetime, higher concentration of extracted charges, and an extended exponential tail, as indicated in **Figure 4f**. Moreover, the lead perovskite demonstrates a larger total extracted charge, Q_{ex} , calculated as the surface area under $n_{ex}(t)$ and $p_{ex}(t)$, as summarized in **Figure 4d**. Interestingly, the total extracted charge in the lead perovskite system are nearly balanced, with $Q_e/Q_h = 2$. However, a much more significant difference is observed in the tin perovskite system, with $Q_e/Q_h = 14.5$. Additionally, the tin perovskite system loses a considerable amount of charges. Specifically, the ETL extracts 30 times fewer electrons, and the HTL extracts 160 fewer holes than the lead perovskite system. This significant reduction in extracted charge highlights the poor capabilities of tin perovskite solar cell interfaces in extracting both holes and electrons, as well as large recombination losses.

After demonstrating the humble charge extraction capabilities of tin perovskites compared to lead-perovskite interfaces. Next, we quantify the impact of each recombination channel on the extracted charges. Three factors can influence the extracted charges: the extraction rate constant (rate constant deficit), nonradiative recombination, and radiative recombination. We will now examine the effect of each of these factors on the extracted charge and compare the extraction and losses of both holes and electrons. We found that tin perovskites exhibit lower charge extraction constants, as illustrated in **Figure 4g**. The rate constraints for the HTL and ETL are 33 and 12 times lower than rate constraints in Pb perovskite interfaces. This difference may arise from the energetic misalignment between the absorber layer and the CTLs, as highlighted by the KP-PYS data shown in **Figure 1**. Alternatively, it could be attributed to the damage on the perovskite surface, resulting in a poorly aligned interface with the CTL. We consider the charge extracted from lead perovskite as the baseline and examine the impact of factors affecting charge extraction (extraction constant deficit, nonradiative recombination, and radiative recombination) one by one to assess their influence on charge losses, which would reveal a road map to tackle the energy bands misalignment challenge in tin perovskites. The charge losses are depicted in **Figure 4h and i**, where 100% represents the electron and hole charge from **Figure 4d**, respectively. The charge loss percentage is calculated using the formula $loss = (Q_{lead} - Q_{tin}) / Q_{lead}$

In both ETLs and HTLs, the primary source of charge loss is nonradiative recombination, accounting for 90% of the charge loss in the ETL interface and 99% in the HTL interface. This slightly higher loss percentage at the HTL interface can be attributed to the larger surface recombination, as indicated in **Tables S1-2**. The extraction rate constant deficit contributes to 70% and 60% of charge loss in the ETL and HTL interfaces, respectively. Interestingly, in the HTL interface, the high material doping ($1.5 \times 10^{17} \text{ cm}^{-3}$) results in significant hole losses, with 97% of holes being lost. In contrast, the same doping level in the ETL induces only 28% of electron loss in the tin ETL interface. To identify the reasons for such behavior, we plotted quasi-Fermi level splitting (QFLS) in both lead and tin systems, demonstrating the effect of recombination channels on charge concentration in the perovskite absorber film itself, considering additional ETL and HTL surface recombination (**Figure 4j**). Due to the significantly enhanced passivation capability of 2PACz in lead perovskites, QFLS reaches a value of 1 eV

(after recalculation of QFLS to the bandgap of FASnI_3), which is very close to the Shockley-Queisser limit of 1.1 eV in FASnI_3 . In contrast, the C_{60} ETL interface is more susceptible to nonradiative recombination, resulting in a QFLS of 0.84 eV. Consequently, doping and radiative recombination substantially influence the charge extraction potential in the HTL interface in tin perovskites compared to the ETL interface.

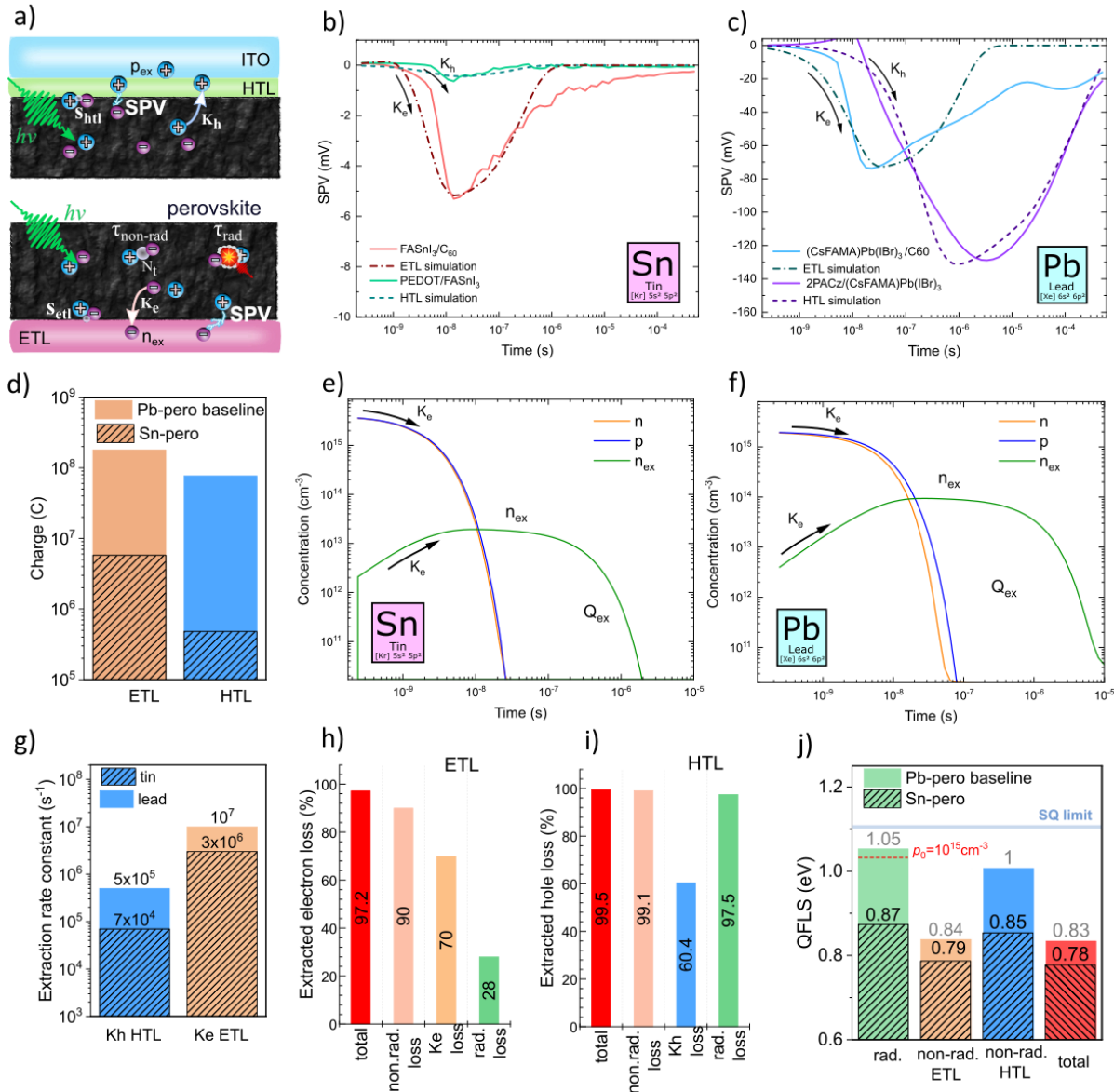


Figure 4. Non-radiative recombination is the main charge loss channel in Sn-based perovskite solar cells according to simulation of charge extraction and charge losses in FASnI_3 and $(\text{Cs}_{0.05}\text{FA}_{0.855}\text{MA}_{0.095})\text{Pb}(\text{I}_{0.9}\text{Br}_{0.1})_3$ perovskite systems. (a) A theoretical model describing charge extraction. (b) Fitting of experimental data in tin perovskites ETLs and HTLs interfaces. (c) Fitting of experimental data in lead perovskite ETL and HTL interfaces. (d) Total electron and hole charge extracted by HTL and ETL per one laser pulse. (e) and (f) Time evolution of electron and hole concentrations in the perovskite layer, along with the evolution of extracted electrons in the tin and lead systems, respectively. (g) Hole and electron extraction rate constants. (h) and (i) Loss of extracted electrons and holes induced by nonradiative recombination, and (j) QFLS (eV) for different recombination channels (radiative, non-radiative) in the ETL and HTL, along with the total QFLS and the Shockley-Queisser (SQ) limit.

extraction constant deficit, and radiative recombination in the ETL and HTL, respectively, using the charge in the Pb system as a baseline. (j) Quasi-Fermi Level Splitting (QFLS) affected by nonradiative and radiative recombination channels.

To achieve the baseline performance of lead perovskite (22% efficiency), several key steps must be taken. Firstly, it is crucial to significantly reduce nonradiative recombination and passivate trap states both in the bulk and on the surface of the absorber tin perovskite material. This is necessary to achieve lifetimes in the microsecond range, similar to those observed in lead perovskites. Secondly, the background hole density needs to be reduced to at least the level of 10^{15} cm^{-3} . Thirdly, there is a need to improve the alignment of the ETL and HTL to enhance the extraction rate constants, aiming for values around $10^7 \text{ cm}^{-3}\text{s}^{-1}$.

Simulation of tin perovskite solar cell operation:

We have comprehensively studied the factors influencing energy alignment, charge extraction and recombination in tin perovskite interfaces. We further investigated the impact of these limiting factors on a real THPSC device which showed a conversion efficiency of 6%. To model real device, we utilized 2D drift-diffusion simulations under steady-state illumination conditions. Based on the findings of KP and PYS measurements, we modeled the layers of perovskite, C_{60} , and PEDOT as crystalline semiconductors, considering their respective thickness, energy band gap, and affinity. The perovskite p-type doping was set to $1.5 \times 10^{17} \text{ cm}^{-3}$, as determined through multimethod measurements in our study. Additionally, we observed a significant valence band offset (VBO) of approximately 0.47 eV between the perovskite layer and C_{60} .

To facilitate the injection of photogenerated holes from the perovskite to PEDOT via thermionic emission over the barrier, we adjusted the VBM of PEDOT in our model. We increased it by 0.12 eV compared to our experimental data, considering the possibility of defect-assisted tunneling across the barrier. Furthermore, we note that the VBM edge of PEDOT may shift upon the deposition of the perovskite. Schottky contacts were implemented at the C_{60} and PEDOT sides of the solar cell, with corresponding WF values of 3.95 eV and 4.74 eV, measured for ITO and Ag:BCP respectively.

Given the considerable CBO of approximately -0.53 eV between the perovskite and C_{60} , we anticipated significant nonradiative recombination at this interface. To address this issue, we introduced a fictitious layer between the two materials with Shockley-Read-Hall nonradiative recombination. This one nm-thick layer shared the CBM of C_{60} and the VBM of the perovskite, enabling recombination between photogenerated electrons injected in C_{60} and photogenerated holes in the perovskite. This additional layer was necessary to align the V_{oc} of our simulated perovskite solar cell with the experimental data. We report all the material parameters employed to produce the blue JV curve in **Figure 5 and Table S5**, together with the experimental curve (black line).

Figure 5b illustrates the equilibrium band diagram of the material stack. As mentioned earlier, a significant cliff at the FASnI₃/C₆₀ interface limits the maximum achievable V_{oc}. Since the perovskite doping density exceeds that of C₆₀, most of the built-in voltage drops across the C₆₀ film, resulting in an ineffective separation of photogenerated carriers, meaning that carrier separation in the tin perovskite film is impossible. Notably, the majority of carriers are generated near the FASnI₃/PEDOT interface, where a field-free region is present. This can potentially hinder charge collection and hole extraction, considering the low lifetime of the free carriers in FASnI₃. If the solar cell were illuminated from the ETL side, most of the electrons would be photogenerated near the C₆₀ interface, reducing bulk nonradiative recombination. **Figure 5a** also contains the JV curve obtained by the same parameter choice as in the PPN suggested configuration, where the material stack is illuminated from the C₆₀ side (orange curve) to test NPP solar cell architecture feasibility. We found that NPP architecture delivers 16% larger PCE value compared to PPN structure (PCE_{NPP} = 7.2 % compared to PCE_{PPN} = 6.2 %).

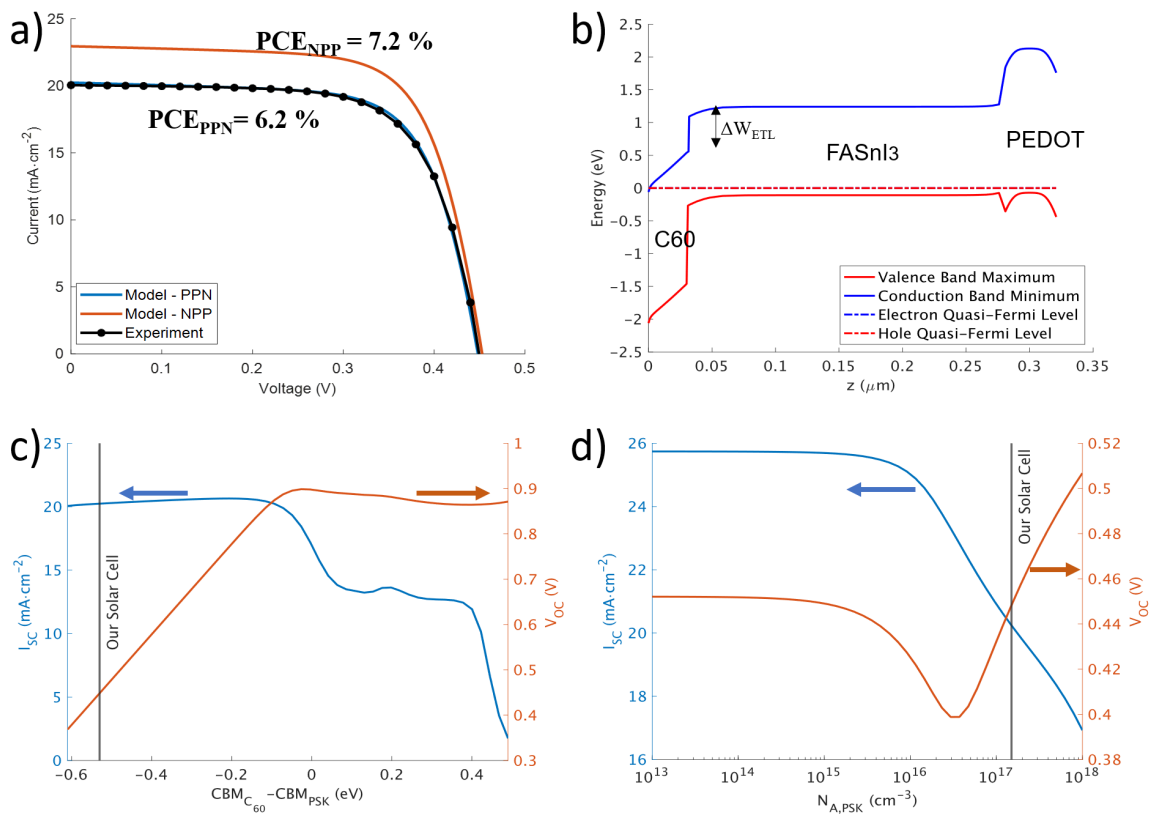


Figure 5: CBO, non-radiative recombination, and doping limits FASnI₃ Solar Cell Performance in PPN and NPP architecture (a) JV curve of the simulated solar cell in PPN and NPP configuration with respect to the experimental JV curve. (b) Equilibrium band diagram of the solar cell employing the parameters listed in **Table S5**. (c) J_{sc} and V_{oc} of the solar cell as a function of the conduction band offset between the perovskite and C₆₀ (c), and as a function of the perovskite p-type doping (d).

After achieving a satisfactory fit for the JV curve, we explored variations of energy offset, doping, and recombination rate on tin perovskite's efficiency demonstrating the room for further THPSCs improvement. First of all, we focused on the CBO at the C₆₀/FASnI₃ interface. **Figure 5c** demonstrates how THPSCs would perform if we mitigate the large CBO. Starting from the conditions indicated by the solid black vertical line ($\Delta W_{\text{ETL}} = \text{CBM}_{\text{C60}} - \text{CBM}_{\text{PSK}} = -0.53$ eV), J_{SC} would not degrade significantly while V_{OC} would nearly double, up until $\text{CBM}_{\text{C60}} \approx \text{CBM}_{\text{PSK}} - 0.1$ eV. Increasing the interface bandgap between the materials would reduce nonradiative recombination at the interface, benefiting V_{oc}. Importantly, this improvement can be achieved without decreasing the nonradiative lifetime of the interface layer (or its trap density), which we maintained at 1.5 ns in our simulations. If the CBO increases further, a barrier for electron extraction emerges, severely degrading J_{SC} while leaving V_{oc} unaffected, as determined under zero-current conditions.

Next, we consider the effect of p-type doping density on THPSC J_{sc} and V_{oc}. Starting from the experimental found concentration indicated by the solid black vertical line ($N_{\text{A, PSK}} = 1.5 \times 10^{17}$ cm⁻³), reducing the perovskite doping to values below 10¹⁶ cm⁻³ establishes a constant electric field throughout the perovskite film. This field improves charge extraction, thereby enhancing J_{sc} and minimizing bulk nonradiative recombination. However, V_{oc} is slightly affected since it is primarily limited by interface recombination. The non-monotonous trend of V_{oc} around 0.4 V can be attributed to two competing phenomena. On the one hand, increased perovskite doping negatively impacts V_{oc}, as explained earlier for J_{sc}. On the other hand, higher perovskite doping values may slightly benefit V_{oc} due to the quenching of interface recombination. As the perovskite doping density increases, the interface Fermi level shifts from values close to the C₆₀ CBM toward the perovskite VBM as illustrated in **Figure SI 13**. When the interface Fermi level approaches midgap, the nonradiative recombination rate at the interface increases since the populations of holes and electrons become comparable.

Conclusion:

In this work, we measured the doping concentration of FASnI₃ using three different techniques and found to be in the range of 1.5×10^{17} cm⁻³. Then we investigated the energy bands alignment profile of FASnI₃ in the most used device stack ITO/PEDOT/FASnI₃/C₆₀/BCP/Ag using PK-PYS setup. We evaluated the energy diagram of the full stack layer by layer to measure the accurate energy position of every layer as close as possible to actual operating conditions. We also highlighted the energy mismatch at the interfaces and introduced an accurate energy band diagram. The role of BCP was also explained, and found to complex with Ag, establishing an intermediate energy level that facilitates electron extraction. Tr-SPV measurements and KP-based SPV measurements confirmed the same results and illustrated the significant effect of BCP in electron extraction.

We also studied the charge extraction dynamics using tr-SPV for the first time in tin halide perovskites. We investigated the extraction dynamics of HTL/FASnI₃ interfaces using PEDOT and NiOx and found that both show very low hole extraction and low selectivity. However, PEDOT shows relatively better hole extraction than NiOx, which was enhanced by adding SnBr₂ to increase the energy band alignment. We also investigated SAMs, and found that it could work as HTL for tin perovskites provided a good energy band alignment. On the other hand, we investigated the electron extraction dynamics and found that C₆₀ and BCPM show better electron extraction than ICBA. Surprisingly, the extraction abilities of the three films followed the charges mobility order rather than the CBO order. This improvement can be achieved by exploring new CTLs or utilizing self-assembled monolayers with shallow energy levels.

Our results can guide the community towards choosing more adapted ETLs for tin perovskites, which possess significantly lower affinity than their lead counterpart. As illustrated earlier, the correct choice of ETL affinity could easily double the cell V_{oc}. Large perovskite P-type doping is also an issue affecting charge extraction and J_{sc}. The NPP solar cell with the same experimentally found characteristics could show a J_{sc} improvement of 2.8 mA/cm². Further reducing of the perovskite p-type doping below 10¹⁵ cm⁻³ would improve J_{sc} by about 5.7 mA/cm². We suggest designing a new charge extraction system well aligned with the tin perovskite film or trying the opposite strategy of controlling the WF of tin perovskites by polar surface additives⁵⁵ to enhance the band alignment with good CTLs such as C₆₀/BCP. The methodology and findings presented in this study can be applied to identify optimal ETL and HTL candidates that can enable tin perovskites to exceed the efficiency threshold of 20%, and increase the commercialization possibilities of such green solar cell material.

References:

- (1) Li, G.; Su, Z.; Canil, L.; Hughes, D.; Aldamasy, M. H.; Dagar, J.; Trofimov, S.; Wang, L.; Zuo, W.; Jerónimo-Rendon, J. J.; Byranvand, M. M.; Wang, C.; Zhu, R.; Zhang, Z.; Yang, F.; Nasti, G.; Naydenov, B.; Tsoi, W. C.; Li, Z.; Gao, X.; Wang, Z.; Jia, Y.; Unger, E.; Saliba, M.; Li, M.; Abate, A. Highly Efficient P-i-n Perovskite Solar Cells That Endure Temperature Variations. *Science (80-.)*. **2023**, 379 (6630), 399–403. https://doi.org/10.1126/SCIENCE.ADD7331/SUPPL_FILE/SCIENCE.ADD7331_SM.PDF.
- (2) Park, J.; Kim, J.; Yun, H. S.; Paik, M. J.; Noh, E.; Mun, H. J.; Kim, M. G.; Shin, T. J.; Seok, S. Il. Controlled Growth of Perovskite Layers with Volatile Alkylammonium Chlorides. *Nat. 2023 6167958* **2023**, 616 (7958), 724–730. <https://doi.org/10.1038/s41586-023-05825-y>.
- (3) Abate, A. Perovskite Solar Cells Go Lead Free. <https://doi.org/10.1016/j.joule.2017.09.007>.
- (4) Wang, X.; Dong, B.; Feng, M.; Xue, D. J.; Wang, S. M. Sustainable Management of Lead in Perovskite Solar Cells. *J. Mater. Chem. A* **2022**, 10 (30), 15861–15864. <https://doi.org/10.1039/D2TA03081K>.
- (5) Byranvand, M. M.; Zuo, W.; Imani, R.; Pazoki, M.; Saliba, M. Tin-Based Halide Perovskite Materials: Properties and Applications. *Chem. Sci.* **2022**, 13 (23), 6766–6781. <https://doi.org/10.1039/D2SC01914K>.
- (6) Treglia, A.; Ambrosio, F.; Martani, S.; Folpini, G.; Barker, A. J.; Albaqami, M. D.; De Angelis, F.; Poli, I.;

- Petrozza, A. Effect of Electronic Doping and Traps on Carrier Dynamics in Tin Halide Perovskites. *Mater. Horizons* **2022**, *9* (6), 1763–1773. <https://doi.org/10.1039/D2MH00008C>.
- (7) Tao, S.; Schmidt, I.; Brocks, G.; Jiang, J.; Tranca, I.; Meerholz, K.; Olthof, S. Absolute Energy Level Positions in Tin- and Lead-Based Halide Perovskites. *Nat. Commun.* **2019**, *10* (1), 1–10. <https://doi.org/10.1038/s41467-019-10468-7>.
- (8) Gao, W.; Li, P.; Chen, J.; Ran, C.; Wu, Z. Interface Engineering in Tin Perovskite Solar Cells. *Adv. Mater. Interfaces* **2019**, *6* (24), 1901322. <https://doi.org/10.1002/ADMI.201901322>.
- (9) Hellmann, T.; Wussler, M.; Das, C.; Dachauer, R.; El-Helaly, I.; Mortan, C.; Mayer, T.; Jaegermann, W. The Difference in Electronic Structure of MAPI and MASI Perovskites and Its Effect on the Interface Alignment to the HTMs Spiro-MeOTAD and Cul. *J. Mater. Chem. C* **2019**, *7* (18), 5324–5332. <https://doi.org/10.1039/C8TC06332J>.
- (10) Chen, N.; Luo, D.; Chen, P.; Li, S.; Hu, J.; Wang, D.; Zhu, R.; Lu, Z.-H. Universal Band Alignment Rule for Perovskite/Organic Heterojunction Interfaces. *ACS Energy Lett.* **2023**, 1313–1321. <https://doi.org/10.1021/ACSENERGYLETT.2C02856>.
- (11) Hussein, M.; Iqbal, Z.; Li, G.; Pascual, J.; Alharthi, F.; Abate, A.; Li, M. Challenges in Tin Perovskite Solar Cells. *Phys. Chem. Chem. Phys.* **2021**. <https://doi.org/10.1039/D1CP02596A>.
- (12) Liu, H.; Zhang, Z.; Zuo, W.; Roy, R.; Li, M.; Byranvand, M. M.; Saliba, M. Pure Tin Halide Perovskite Solar Cells: Focusing on Preparation and Strategies. *Adv. Energy Mater.* **2022**, 2202209. <https://doi.org/10.1002/AENM.202202209>.
- (13) Lee, M.; Kim, D.; Lee, Y. K.; Koo, H.; Lee, K. T.; Chung, I. Indene-C60Bisadduct Electron-Transporting Material with the High LUMO Level Enhances Open-Circuit Voltage and Efficiency of Tin-Based Perovskite Solar Cells. *ACS Appl. Energy Mater.* **2020**, *3* (6), 5581–5588. https://doi.org/10.1021/ACSAEM.0C00535/ASSET/IMAGES/LARGE/AE0C00535_0004.JPEG.
- (14) Zhou, J.; Hao, M.; Zhang, Y.; Ma, X.; Dong, J.; Lu, F.; Wang, J.; Wang, N.; Zhou, Y. Chemo-Thermal Surface Dedoping for High-Performance Tin Perovskite Solar Cells. *Matter* **2022**. <https://doi.org/10.1016/J.MATT.2021.12.013>.
- (15) Yu, B.-B.; Chen, Z.; Zhu, Y.; Wang, Y.; Han, B.; Chen, G.; Zhang, X.; Du, Z.; He, Z.; Yu, B.-B.; Zhu, Y.; Wang, Y.; Han, B.; Chen, G.; Zhang, X.; Du, Z.; He, Z.; Chen, Z. Heterogeneous 2D/3D Tin-Halides Perovskite Solar Cells with Certified Conversion Efficiency Breaking 14%. *Adv. Mater.* **2021**, *33* (36), 2102055. <https://doi.org/10.1002/ADMA.202102055>.
- (16) Chen, Y.; Wang, K.; Qi, H.; Zhang, Y.; Wang, T.; Tong, Y.; Wang, H. Mitigating Voc Loss in Tin Perovskite Solar Cells via Simultaneous Suppression of Bulk and Interface Nonradiative Recombination. *ACS Appl. Mater. Interfaces* **2022**. <https://doi.org/10.1021/ACSAMI.2C12129>.
- (17) Chen, M.; Kapil, G.; Wang, L.; Razey Sahamir, S.; Baranwal, A. K.; Nishimura, K.; Sanehira, Y.; Zhang, Z.; Akmal Kamarudin, M.; Shen, Q.; Hayase, S. High Performance Wide Bandgap Lead-Free Perovskite Solar Cells by Monolayer Engineering. *Chem. Eng. J.* **2022**, *436*, 135196. <https://doi.org/10.1016/J.CEJ.2022.135196>.
- (18) Wu, T.; Cui, D.; Liu, X.; Meng, X.; Wang, Y.; Noda, T.; Segawa, H.; Yang, X.; Zhang, Y.; Han, L. Efficient and Stable Tin Perovskite Solar Cells Enabled by Graded Heterostructure of Light-Absorbing Layer. *Sol. RRL* **2020**, *4* (9), 2000240. <https://doi.org/10.1002/SOLR.202000240>.
- (19) Li, P.; Dong, H.; Li, J.; Cao, X.; Xi, J.; Wang, D.; Jiao, B.; Hou, X.; Yang, Y.; Wu, Z. Synergistic Trifluoroacetamide Regulating Crystal Orientation and Energy Alignment for Tin-Based Perovskite Solar Cells. *Org. Electron.* **2023**, *113*, 106707. <https://doi.org/10.1016/J.ORGEL.2022.106707>.

- (20) Li, H.; Chang, B.; Wang, L.; Wang, Z.; Pan, L.; Wu, Y.; Liu, Z.; Yin, L. Surface Reconstruction for Tin-Based Perovskite Solar Cells. *ACS Energy Lett.* **2022**, *14*, 3889–3899. https://doi.org/10.1021/ACSENERGYLETT.2C01624/ASSET/IMAGES/LARGE/NZ2C01624_0005.JPEG.
- (21) Li, B.; Wu, X.; Zhang, H.; Zhang, S.; Li, Z.; Gao, D.; Zhang, C.; Chen, M.; Xiao, S.; Jen, A. K.-Y.; Yang, S.; Zhu, Z. Efficient and Stable Tin Perovskite Solar Cells by Pyridine-Functionalized Fullerene with Reduced Interfacial Energy Loss. *Adv. Funct. Mater.* **2022**, 2205870. <https://doi.org/10.1002/ADFM.202205870>.
- (22) Zhang, Z.; Kamarudin, M. A.; Baranwal, A. K.; Kapil, G.; Sahamir, S. R.; Sanehira, Y.; Chen, M.; Wang, L.; Shen, Q.; Hayase, S. Sequential Passivation for Lead-Free Tin Perovskite Solar Cells with High Efficiency. *Angew. Chemie* **2022**, *134* (42), e202210101. <https://doi.org/10.1002/ANGE.202210101>.
- (23) Rono, N.; Merad, A. E.; Kibet, J. K.; Martincigh, B. S.; Nyamori, V. O. A Theoretical Investigation of the Effect of the Hole and Electron Transport Materials on the Performance of a Lead-Free Perovskite Solar Cell Based on CH₃NH₃SnI₃. *J. Comput. Electron.* **2021**, *20* (2), 993–1005. <https://doi.org/10.1007/S10825-021-01673-Z/FIGURES/10>.
- (24) Hossain, M. K.; Toki, G. F. I.; Kuddus, A.; Rubel, M. H. K.; Hossain, M. M.; Bencherif, H.; Rahman, M. F.; Islam, M. R.; Mushtaq, M. An Extensive Study on Multiple ETL and HTL Layers to Design and Simulation of High-Performance Lead-Free CsSnCl₃-Based Perovskite Solar Cells. *Sci. Reports* **2023**, *13* (1), 1–24. <https://doi.org/10.1038/s41598-023-28506-2>.
- (25) Li, G.; Xu, M.; Chen, Z.; Zou, X. Design and Simulation Investigations on Electron Transport Layer-Free in Tin-Based p-n Homojunction Perovskite Solar Cells. *Mater. Today Commun.* **2023**, *35*, 106232. <https://doi.org/10.1016/J.MTCOMM.2023.106232>.
- (26) Liang, K.; Huang, L.; Wang, T.; Wang, C.; Guo, Y.; Yue, Y.; Liu, X.; Zhang, J.; Hu, Z.; Zhu, Y. Rational Design of Formamidine Tin-Based Perovskite Solar Cell with 30% Potential Efficiency via 1-D Device Simulation. *Phys. Chem. Chem. Phys.* **2023**, *25* (13), 9413–9427. <https://doi.org/10.1039/D2CP05226A>.
- (27) Roy, P.; Raoui, Y.; Khare, A. Design and Simulation of Efficient Tin Based Perovskite Solar Cells through Optimization of Selective Layers: Theoretical Insights. *Opt. Mater. (Amst.)* **2022**, *125*, 112057. <https://doi.org/10.1016/J.OPTMAT.2022.112057>.
- (28) Abdelaziz, S.; Zekry, A.; Shaker, A.; Abouelatta, M. Investigating the Performance of Formamidinium Tin-Based Perovskite Solar Cell by SCAPS Device Simulation. *Opt. Mater. (Amst.)* **2020**, *101*, 109738. <https://doi.org/10.1016/J.OPTMAT.2020.109738>.
- (29) Lee, Y. J.; Wang, J.; Hsu, J. W. P. Surface Photovoltage Characterization of Organic Photovoltaic Devices. *Appl. Phys. Lett.* **2013**, *103* (17), 173302. <https://doi.org/10.1063/1.4827104>.
- (30) Cavalcoli, D.; Cavallini, A. Surface Photovoltage Spectroscopy -Method and Applications. *Phys. Status Solidi Curr. Top. Solid State Phys.* **2010**, *7* (5), 1293–1300. <https://doi.org/10.1002/PSSC.200983124>.
- (31) *Surface Photovoltage Analysis of Photoactive Materials - Thomas Dittrich, Steffen Fengler - Google Books.* https://books.google.de/books?hl=en&lr=&id=-LnVDwAAQBAJ&oi=fnd&pg=PR5&ots=VO-hCFMlkc&sig=4xjH2GT5vvlIOxNAtRexWE9kfHM&redir_esc=y#v=onepage&q&f=false (accessed 2023-02-20).
- (32) Levine, I.; Al-Ashouri, A.; Musiienko, A.; Hempel, H.; Magomedov, A.; Drevilkauskaitė, A.; Getautis, V.; Menzel, D.; Hinrichs, K.; Unold, T.; Albrecht, S.; Dittrich, T. Charge Transfer Rates and Electron Trapping at Buried Interfaces of Perovskite Solar Cells. *Joule* **2021**, *5* (11), 2915–2933. <https://doi.org/10.1016/J.JOULE.2021.07.016>.
- (33) Jiang, X.; Zang, Z.; Zhou, Y.; Li, H.; Wei, Q.; Ning, Z. Tin Halide Perovskite Solar Cells: An Emerging Thin-

Film Photovoltaic Technology. *Accounts Mater. Res.* **2021**, *2* (4), 210–219.
https://doi.org/10.1021/ACCOUNTSMR.0C00111/ASSET/IMAGES/LARGE/MR0C00111_0005.JPEG.

- (34) Drago, R. S. Thermodynamic Evaluation of the Inert Pair Effect. *Journal of Physical Chemistry*. American Chemical Society 1958, pp 353–357. <https://doi.org/10.1021/j150561a027>.
- (35) Peng, L.; Xie, W. Theoretical and Experimental Investigations on the Bulk Photovoltaic Effect in Lead-Free Perovskites MASnI₃ and FASnI₃. *RSC Adv.* **2020**, *10* (25), 14679–14688.
<https://doi.org/10.1039/D0RA02584D>.
- (36) Rusu, M.; Kodalle, T.; Choubrac, L.; Barreau, N.; Kaufmann, C. A.; Schlatmann, R.; Unold, T. Electronic Structure of the CdS/Cu(In,Ga)Se₂ Interface of KF- and RbF-Treated Samples by Kelvin Probe and Photoelectron Yield Spectroscopy. *Cite This ACS Appl. Mater. Interfaces* **2021**, *13*, 7755.
<https://doi.org/10.1021/acsami.0c20976>.
- (37) Liu, X.; Wu, T.; Zhang, C.; Zhang, Y.; Segawa, H.; Han, L.; Liu, X.; Segawa, H.; Han, L.; Wu, T.; Zhang, C.; Zhang, Y. Interface Energy-Level Management toward Efficient Tin Perovskite Solar Cells with Hole-Transport-Layer-Free Structure. *Adv. Funct. Mater.* **2021**, *31* (50), 2106560.
<https://doi.org/10.1002/ADFM.202106560>.
- (38) Pitaro, M.; Kinsa Tekelenburg, E.; Shao, S.; Antonietta Loi, M.; Pitaro, M.; Tekelenburg, E. K.; Shao, S.; Loi Photophysics, M. A. Tin Halide Perovskites: From Fundamental Properties to Solar Cells. *Adv. Mater.* **2022**, *34* (1), 2105844. <https://doi.org/10.1002/ADMA.202105844>.
- (39) Wu, Y.; Chen, W.; Lin, Y.; Tu, B.; Lan, X.; Wu, Z.; Liu, R.; Djurišić, A. B.; He, Z. B. General Method to Define the Type of Carrier Transport Materials for Perovskite Solar Cells via Kelvin Probes Microscopy. *ACS Appl. Energy Mater.* **2018**, *1* (8), 3984–3991.
https://doi.org/10.1021/ACSAEM.8B00687/ASSET/IMAGES/LARGE/AE-2018-006879_0005.JPEG.
- (40) Siekmann, J.; Kulkarni, A.; Akel, S.; Klingebiel, B.; Saliba, M.; Rau, U.; Kirchartz, T. Characterizing the Influence of Charge Extraction Layers on the Performance of Triple-Cation Perovskite Solar Cells. *Adv. Energy Mater.* **2023**, *13* (32), 2300448. <https://doi.org/10.1002/AENM.202300448>.
- (41) Kavadiya, S.; Onno, A.; Boyd, C. C.; Wang, X.; Cetta, A.; McGehee, M. D.; Holman, Z. C. Investigation of the Selectivity of Carrier Transport Layers in Wide-Bandgap Perovskite Solar Cells. *Sol. RRL* **2021**, *5* (7), 2100107. <https://doi.org/10.1002/SOLR.202100107>.
- (42) Zhu, H. L.; Cheng, J.; Zhang, D.; Liang, C.; Reckmeier, C. J.; Huang, H.; Rogach, A. L.; Choy, W. C. H. Room-Temperature Solution-Processed NiOx:PbI₂ Nanocomposite Structures for Realizing High-Performance Perovskite Photodetectors. *ACS Nano* **2016**, *10* (7), 6808–6815.
https://doi.org/10.1021/ACSNANO.6B02425/ASSET/IMAGES/LARGE/NN-2016-02425S_0006.JPEG.
- (43) Liu, Y.; Qi, J.; Peng, X.; Cao, Y. Alcohol Soluble Porphyrin for the Cathode Buffer Layers of Fullerene/Perovskite Planar Heterojunction Solar Cells. *Org. Electron.* **2018**, *59*, 414–418.
<https://doi.org/10.1016/J.ORGEL.2018.05.045>.
- (44) Yang, Z.; Babu, B. H.; Wu, S.; Liu, T.; Fang, S.; Xiong, Z.; Han, L.; Chen, W. Review on Practical Interface Engineering of Perovskite Solar Cells: From Efficiency to Stability. *Sol. RRL* **2020**, *4* (2), 1900257.
<https://doi.org/10.1002/SOLR.201900257>.
- (45) Nishimura, K.; Kamarudin, M. A.; Hirotsu, D.; Hamada, K.; Shen, Q.; Iikubo, S.; Minemoto, T.; Yoshino, K.; Hayase, S. Lead-Free Tin-Halide Perovskite Solar Cells with 13% Efficiency. *Nano Energy* **2020**, *74*, 104858. <https://doi.org/10.1016/J.NANOEN.2020.104858>.
- (46) Ying, Z.; Yang, X.; Zheng, J.; Sun, J.; Xiu, J.; Zhu, Y.; Wang, X.; Chen, Y.; Li, X.; Sheng, J.; Shou, C.; Zeng, Y.; Pan, H.; Ye, J.; He, Z. Bathocuproine:Ag Complex Functionalized Tunneling Junction for Efficient Monolithic Perovskite/TOPCon Silicon Tandem Solar Cell. *Sol. RRL* **2022**, *6* (12), 2200793.

<https://doi.org/10.1002/SOLR.202200793>.

- (47) Ying, Z.; Yang, X.; Zheng, J.; Zhu, Y.; Xiu, J.; Chen, W.; Shou, C.; Sheng, J.; Zeng, Y.; Yan, B.; Pan, H.; Ye, J.; He, Z. Charge-Transfer Induced Multifunctional BCP:Ag Complexes for Semi-Transparent Perovskite Solar Cells with a Record Fill Factor of 80.1%. *J. Mater. Chem. A* **2021**, *9* (20), 12009–12018. <https://doi.org/10.1039/D1TA01180D>.
- (48) Wang, S.; Sakurai, T.; Hao, X.; Fu, W.; Masuda, S.; Akimoto, K. Favorable Electronic Structure for Organic Solar Cells Induced by Strong Interaction at Interface. *J. Appl. Phys.* **2013**, *114* (18), 183707. <https://doi.org/10.1063/1.4829905>.
- (49) Chen, K.; Wu, P.; Yang, W.; Su, R.; Luo, D.; Yang, X.; Tu, Y.; Zhu, R.; Gong, Q. Low-Dimensional Perovskite Interlayer for Highly Efficient Lead-Free Formamidinium Tin Iodide Perovskite Solar Cells. *Nano Energy* **2018**, *49*, 411–418. <https://doi.org/10.1016/J.NANOEN.2018.05.006>.
- (50) Shih, C.-C.; Wu, C.-G. Synergistic Engineering of the Conductivity and Surface Properties of PEDOT:PSS-Based HTLs for Inverted Tin Perovskite Solar Cells to Achieve Efficiency over 10%. *ACS Appl. Mater. Interfaces* **2022**. <https://doi.org/10.1021/ACSAMI.1C22262>.
- (51) Donchev, V. Surface Photovoltage Spectroscopy of Semiconductor Materials for Optoelectronic Applications. *Mater. Res. Express* **2019**, *6* (10), 103001. <https://doi.org/10.1088/2053-1591/AB3BF0>.
- (52) Song, D.; Narra, S.; Li, M. Y.; Lin, J. S.; Diao, E. W. G. Interfacial Engineering with a Hole-Selective Self-Assembled Monolayer for Tin Perovskite Solar Cells via a Two-Step Fabrication. *ACS Energy Lett.* **2021**, *6* (12), 4179–4186. https://doi.org/10.1021/ACSENERGYLETT.1C02124/SUPPL_FILE/NZ1C02124_SI_001.PDF.
- (53) Liang, P. W.; Chueh, C. C.; Williams, S. T.; Jen, A. K. Y. Roles of Fullerene-Based Interlayers in Enhancing the Performance of Organometal Perovskite Thin-Film Solar Cells. *Adv. Energy Mater.* **2015**, *5* (10), 1402321. <https://doi.org/10.1002/AENM.201402321>.
- (54) Kafedjiska, I.; Levine, I.; Musiienko, A.; Maticiu, N.; Bertram, T.; Al-Ashouri, A.; Kaufmann, C. A.; Albrecht, S.; Schlatmann, R.; Lauer, I. Advanced Characterization and Optimization of NiO_x:Cu-SAM Hole-Transporting Bi-Layer for 23.4% Efficient Monolithic Cu(In,Ga)Se₂-Perovskite Tandem Solar Cells. *Adv. Funct. Mater.* **2023**, *33* (34), 2302924. <https://doi.org/10.1002/ADFM.202302924>.
- (55) Canil, L.; Cramer, T.; Fraboni, B.; Ricciarelli, D.; Meggiolaro, D.; Singh, A.; Liu, M.; Rusu, M.; Wolff, C. M.; Phung, N.; Wang, Q.; Neher, D.; Unold, T.; Vivo, P.; Gagliardi, A.; De Angelis, F.; Abate, A. Tuning Halide Perovskite Energy Levels. *Energy Environ. Sci.* **2021**, *14* (3), 1429–1438. <https://doi.org/10.1039/D0EE02216K>.